



An efficient boundary collocation scheme for transient thermal analysis in large-size-ratio functionally graded materials under heat source load

Qiang Xi² · Zhuo-Jia Fu^{1,2,3} · Timon Rabczuk^{2,4}

Received: 6 September 2018 / Accepted: 27 March 2019 / Published online: 9 April 2019
© Springer-Verlag GmbH Germany, part of Springer Nature 2019

Abstract

This paper presents a boundary collocation scheme for transient thermal analysis in large-size-ratio functionally graded materials (FGMs) with heat source load. In the proposed scheme, Laplace transformation and the numerical inverse Laplace transformation (NILT) are implemented to avoid the troublesome time-stepping effect on numerical efficiency. The collocation Trefftz method (CTM) coupled with composite multiple reciprocity method is used to obtain the high accurate results in the solution of nonhomogeneous problems in Laplace-space domain. The extended precision arithmetic is introduced to overcome the ill-posed issues generated from the CTM simulation, the NILT process and the large-size-ratio FGM. Heuristic error analysis and numerical investigation are presented to demonstrate the effectiveness of the proposed scheme for transient thermal analysis. Several benchmark examples are considered under large-size-ratio FGMs with some specific spatial variations (quadratic, exponential and trigonometric functions). The proposed scheme is validated in comparison with known analytical solutions and COMSOL simulation.

Keywords Collocation Trefftz scheme · Numerical inverse Laplace transformation · Extended precision arithmetic · Transient thermal analysis · Large size ratio

1 Introduction

Owing to their excellent thermal properties, functionally graded materials (FGMs) [1–3] have been widely used in the high temperature environments such as aerospace, oil exploration, power generation and so on. With ever-increasing demand on engineering structure performances, great attentions have been focused on thermal analysis of large-size-ratio FGM structures, such as large-aspect-ratio

FGMs (3D cuboid) and the FGMs consisting of the size-disparity components (airplane) as shown in Fig. 1.

For transient thermal analysis [4–6], several temporal discretization schemes and spatial discretization schemes can be selected. The most popular temporal discretization schemes are the time-stepping method [7–9], Laplace transformation technique [10, 11], the spectral collocation methods [12] and convolution quadrature method [13–15]. The spatial discretization schemes mainly include finite difference method [16, 17], finite element method (FEM) [18–20], boundary element method (BEM) [21–23], singular boundary method [24–26], weak-form meshless methods [27–31] and strong-form meshless methods [32–36] and so on. Any combination of these two discretization schemes can constitute a class of methods for simulating the transient thermal behavior under FGMs.

However, the accurate and efficient analysis of transient thermal problems exhibiting large-size-ratio FGM structures or the structures including sharp thermal gradients is currently an open issue of research in computational mechanics community. Very few studies have been reported on this topic. Recently, O'Hara et al. [37] proposed an

✉ Zhuo-Jia Fu
paul212063@hhu.edu.cn

¹ Key Laboratory of Coastal Disaster and Defence, Ministry of Education, Hohai University, Nanjing 210098, China

² Center for Numerical Simulation Software in Engineering and Sciences, College of Mechanics and Materials, Hohai University, Nanjing 211100, China

³ State Key Laboratory of Structural Analysis for Industrial Equipment, Dalian University of Technology, Dalian 116024, China

⁴ Institute of Structural Mechanics, Bauhaus-University Weimar, Weimar 99423, Germany

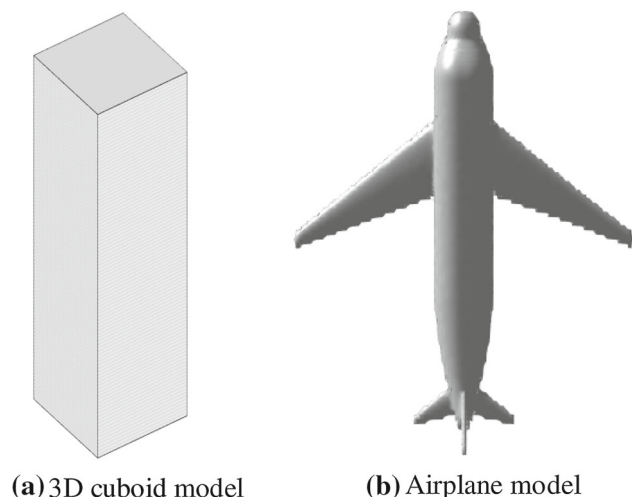


Fig. 1 Typical examples on large-size-ratio FGM structures

advanced FEM with global–local enrichment functions and multi-scale scheme to analyze the transient thermal behavior under the structures including sharp thermal gradients. Some researchers introduced transformation technique or element-subdivision method into the BEM for simulating the thermal behavior under slender structures [38–40]. The authors proposed Laplace-transform boundary knot method in conjunction with extended precision arithmetic (EPA) [41, 42] for solving the transient thermal problems under slender FGMs with exponential variations [43]. It should be mentioned that the aforementioned first two schemes require the modification of the core algorithm to thermal simulation under large-size-ratio FGMs. The third scheme with the EPA is free for the modification of the core algorithm. However, it is restricted to the slender exponential FGMs without heat source loading.

In this study, a Trefftz-based collocation scheme [44, 45] is presented to transient thermal analysis in large-size-ratio FGMs with some specific spatial variations (quadratic, exponential and trigonometric functions [46, 47]) under heat source loading [48]. In the present scheme, it implements Laplace transformation technique to obtain series of the corresponding time-independent nonhomogeneous problems in Laplace-space domain. And then it employs the collocation Trefftz scheme in conjunction with composite multiple reciprocity technique [49, 50] to solve these Laplace-transformed nonhomogeneous problems with boundary-only collocation. Finally, the Fixed Talbot numerical inverse Laplace transform (NILT) [51] is implemented to retrieve the time-dependent numerical solutions of transient thermal conduction equations from the corresponding Laplace-domain solutions. Moreover, the extended precision arithmetic is introduced to alleviate the effect of the ill-posed issues generated from the CTM simulation, the NILT process and the large-size-ratio FGM.

A brief outline of the paper is as follows. In Sect. 2, the collocation scheme including the collocation Trefftz method in conjunction with composite multiple reciprocity method, Laplace transformation and the extended precision arithmetic (EPA) is introduced, and the heuristic error analysis of the proposed collocation scheme is presented. Section 3 investigates the numerical efficiency of the proposed approaches through several typical benchmark examples. Finally, some conclusions are presented in Sect. 4.

2 Methodology

2.1 Mathematical model

Consider transient thermal conduction problems in functionally graded materials under heat source load. The governing equation is stated as

$$\nabla \cdot [\mathbf{K}(\mathbf{x})\nabla u(\mathbf{x}, t)] + Q(\mathbf{x}, t) = \rho(\mathbf{x})c(\mathbf{x})\frac{\partial u(\mathbf{x}, t)}{\partial t}, \quad \mathbf{x} \in \Omega \quad (1)$$

with the boundary and initial conditions:

Dirichlet/Essential condition

$$u(\mathbf{x}, t) = g_1(\mathbf{x}, t), \quad \mathbf{x} \in \Gamma_D \quad (2a)$$

Neumann/Natural condition

$$q(\mathbf{x}, t) = -\mathbf{K}\nabla u(\mathbf{x}, t) \cdot \mathbf{n} = g_2(\mathbf{x}, t), \quad \mathbf{x} \in \Gamma_N \quad (2b)$$

Initial condition

$$u(\mathbf{x}, 0) = u_0(\mathbf{x}), \quad \mathbf{x} \in \Omega \quad (2c)$$

where $\Omega \subset \mathbb{R}^d$ represents a large-size-ratio domain bounded by its boundary Γ , d is the dimension of the computational domain, $u(\mathbf{x}, t)$ is the temperature on the coordinate \mathbf{x} at time instant t , $\Gamma = \Gamma_D \cup \Gamma_N$, $\mathbf{n} = \{n_i\}$ represents the outward unit normal vector at boundary $\mathbf{x} \in \Gamma$, $g_1(\mathbf{x}, t)$, $g_2(\mathbf{x}, t)$ and $u_0(\mathbf{x})$ are known functions. $\mathbf{K} = \{K_{ij}(\mathbf{x})\}_{1 \leq i, j \leq d}$, $\rho(\mathbf{x})$ and $c(\mathbf{x})$ denote the thermal conductivity matrix, the mass density and the specific heat, respectively.

In this study, we assume that the thermal conductivity and the product of mass density and specific heat are, respectively, expressed by

$$K_{ij}(\mathbf{x}) = k_{ij}f(\mathbf{x}), \quad \mathbf{x} \in \Omega, \quad 1 \leq i, \quad j \leq d \quad (3)$$

$$\rho(\mathbf{x})c(\mathbf{x}) = \rho_0c_0f(\mathbf{x}), \quad \mathbf{x} \in \Omega \quad (4)$$

in which $\mathbf{k} = \{k_{ij}\}_{1 \leq i, j \leq d}$ ($\Delta_{\mathbf{k}} = \det(\mathbf{k}) > 0$ and $k_{ij} = k_{ji}$), k_{ij} , ρ_0 , c_0 are all real constants, and $f(\mathbf{x})$ is the function of coordinates.

By employing the following variable transformation

$$v(\mathbf{x}, t) = \sqrt{f(\mathbf{x})}u(\mathbf{x}, t) \tag{5}$$

Equations (1)–(2) can be rewritten as

$$\nabla \cdot [\mathbf{k}\nabla v(\mathbf{x}, t)] + \eta v(\mathbf{x}, t) + \frac{Q(\mathbf{x}, t)}{\sqrt{f(\mathbf{x})}} = \rho_0 c_0 \frac{\partial v(\mathbf{x}, t)}{\partial t} \tag{6}$$

$$v(\mathbf{x}, t) = \sqrt{f(\mathbf{x})}g_1(\mathbf{x}, t), \quad \mathbf{x} \in \Gamma_D \tag{7a}$$

$$-\mathbf{k} \left[\sqrt{f(\mathbf{x})} \nabla v(\mathbf{x}, t) - v(\mathbf{x}, t) \nabla \left(\sqrt{f(\mathbf{x})} \right) \right] \cdot \mathbf{n} = g_2(\mathbf{x}, t), \quad \mathbf{x} \in \Gamma_N \tag{7b}$$

$$v(\mathbf{x}, 0) = \sqrt{f(\mathbf{x})}u_0(\mathbf{x}), \quad \mathbf{x} \in \Omega \tag{7c}$$

where

$$\eta = \sum_{i,j=1}^d k_{ij} \left(\frac{\partial f(\mathbf{x})}{\partial x_i} \frac{\partial f(\mathbf{x})}{\partial x_j} - \frac{\partial^2 f(\mathbf{x})}{\partial x_i \partial x_j} \right) \tag{8}$$

Actually, the parameter η in Eq. (8) can be simplified with the following special forms of $f(\mathbf{x})$:

- (i) Quadratic function $f(\mathbf{x}) = \left(b_0 + \sum_{i=1}^d b_i x_i \right)^2$ with arbitrary constants b_0, b_1, \dots, b_d , then $\eta = 0$ can be determined according to Eq. (8).
- (ii) Exponential function $f(\mathbf{x}) = c_1 e^{\sum_{i=1}^d 2\varsigma_i x_i}$ with arbitrary constants $\varsigma_i (i = 1, 2, \dots, d)$, c_1 , then $\eta = -\sum_{i=1}^d \sum_{j=1}^d \varsigma_i k_{ij} \varsigma_j$ can be determined according to Eq. (8)
- (iii) Trigonometric function $f(\mathbf{x}) = \prod_{i=1}^d (d_i \cos(\beta_i x_i) + e_i \sin(\beta_i x_i))^2$ with arbitrary constants $d_i, e_i, \beta_i (i = 1, 2, \dots, d)$, then $\eta = \sum_{i=1}^d k_{ii} \beta_i^2$ can be determined according to Eq. (8) when $k_{ij} = 0 (i \neq j)$.

2.2 Implementation procedure

For solving the transformed Eqs. (6)–(7), the following roadmap is implemented as shown in Fig. 2.

(a) Laplace transformation

Let Laplace transformation (LT) of $v(\mathbf{x}, t)$ be defined as

$$L(v(\mathbf{x}, t)) = \tilde{v}(\mathbf{x}, \varepsilon) = \int_0^\infty v(\mathbf{x}, t) e^{-\varepsilon t} dt \tag{9}$$

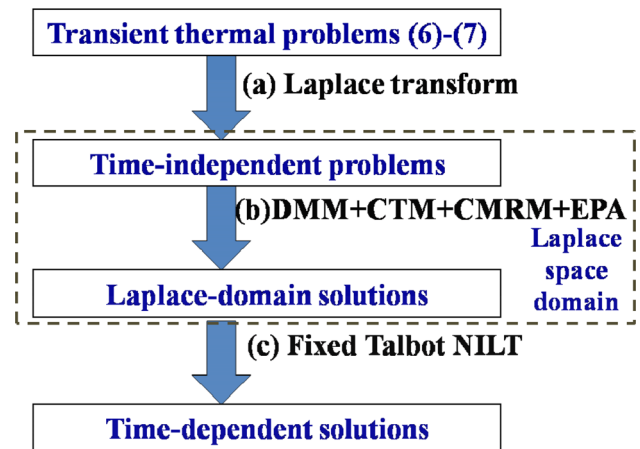


Fig. 2 Roadmaps of the boundary collocation scheme for the problems (6)–(7)

By using Laplace transformation, the transient thermal problems (6)–(7) can be converted from time domain to Laplace-space domain as follows

$$\begin{aligned} \nabla \cdot [\mathbf{k}\nabla \tilde{v}(\mathbf{x}, \varepsilon)] + (\eta - \rho_0 c_0 \varepsilon) \tilde{v}(\mathbf{x}, \varepsilon) \\ = -\rho_0 c_0 v(\mathbf{x}, 0) - \frac{\tilde{Q}(\mathbf{x}, \varepsilon)}{\sqrt{f(\mathbf{x})}} \end{aligned} \tag{10}$$

$$\tilde{v}(\mathbf{x}, \varepsilon) = \sqrt{f(\mathbf{x})} \tilde{g}_1(\mathbf{x}, \varepsilon), \quad \mathbf{x} = (x_1, x_2) \in \Gamma_D \tag{11a}$$

$$-\mathbf{k} \left[\sqrt{f(\mathbf{x})} \nabla \tilde{v}(\mathbf{x}, \varepsilon) - \tilde{v}(\mathbf{x}, \varepsilon) \nabla \left(\sqrt{f(\mathbf{x})} \right) \right] \cdot \mathbf{n} = \tilde{g}_2(\mathbf{x}, \varepsilon), \quad \mathbf{x} = (x_1, x_2) \in \Gamma_N \tag{11b}$$

(b) Boundary collocation technique

To simplify the time-independent nonhomogeneous problems (10)–(11), the domain mapping method (DMM) is introduced. By using the transformation

$$\begin{cases} \begin{pmatrix} y_1 \\ y_2 \end{pmatrix} = \begin{pmatrix} 1/\sqrt{k_{11}} & 0 \\ -k_{12}/\sqrt{k_{11}\Delta_k} & \sqrt{k_{11}}/\sqrt{\Delta_k} \end{pmatrix} \begin{pmatrix} x_1 \\ x_2 \end{pmatrix}, \quad d=2 \\ \begin{pmatrix} y_1 \\ y_2 \\ y_3 \end{pmatrix} = \begin{pmatrix} 1/\sqrt{k_{11}} & 0 & 0 \\ -k_{12}/\sqrt{k_{11}\Delta_k} & \sqrt{k_{11}}/\sqrt{\Delta_k} & 0 \\ \Upsilon_1 & \Upsilon_2 & \Upsilon_3 \end{pmatrix} \begin{pmatrix} x_1 \\ x_2 \\ x_3 \end{pmatrix}, \quad d=3 \end{cases}, \quad \mathbf{y} = \mathbf{k}^{-\mathbf{x}} \tag{12}$$

where $\Upsilon_1 = (k_{12}k_{13} - k_{23}k_{11})\sqrt{k_{11}}/\sqrt{w\Delta_k}$, $\Upsilon_2 = (k_{12}k_{23} - k_{13}k_{22})\sqrt{k_{11}}/\sqrt{w\Delta_k}$, $\Upsilon_3 = \sqrt{k_{11}\Delta_k}/\sqrt{w}$, $w = k_{11}k_{33}\Delta_k - k_{11}k_{22}k_{13}^2 + 2k_{11}k_{12}k_{13}k_{23} - k_{23}^2k_{11}^2$. One may rewrite Eqs. (10)–(11) as the following simplified form in the transformed \mathbf{y} coordinate system

$$\mathfrak{H}\tilde{v}(\mathbf{y}, \varepsilon) = \tilde{W}(\mathbf{y}, \varepsilon) \tag{13}$$

$$\begin{aligned} \tilde{v}(\mathbf{y}, \varepsilon) &= \sqrt{f\left((\mathbf{k}^-)^{-1}\mathbf{y}\right)}\tilde{g}_1\left((\mathbf{k}^-)^{-1}\mathbf{y}, \varepsilon\right) \\ &= D(\mathbf{y}, \varepsilon), \quad \mathbf{y} \in \Gamma_D \end{aligned} \tag{14a}$$

$$\begin{aligned} -\mathbf{k}\left[\sqrt{f\left((\mathbf{k}^-)^{-1}\mathbf{y}\right)}\nabla\tilde{v}(\mathbf{y}, \varepsilon) - \tilde{v}(\mathbf{y}, \varepsilon)\nabla\left(\sqrt{f\left((\mathbf{k}^-)^{-1}\mathbf{y}\right)}\right)\right] \cdot \mathbf{n}, \quad \mathbf{y} \in \Gamma_N \\ = \tilde{g}_2\left((\mathbf{k}^-)^{-1}\mathbf{y}, \varepsilon\right) = E(\mathbf{y}, \varepsilon) \end{aligned} \tag{14b}$$

where $\tilde{W}(\mathbf{y}, \varepsilon) = -\rho_0 c_0 v\left((\mathbf{k}^-)^{-1}\mathbf{y}, 0\right) - \frac{\tilde{Q}\left((\mathbf{k}^-)^{-1}\mathbf{y}, \varepsilon\right)}{\sqrt{f\left((\mathbf{k}^-)^{-1}\mathbf{y}\right)}}$,

and $\mathfrak{H}=(\Delta + \eta - \rho_0 c_0 \varepsilon)$ is a differential operator. If $\eta - \rho_0 c_0 \varepsilon > 0$, \mathfrak{H} is Helmholtz operator; if $\eta - \rho_0 c_0 \varepsilon = 0$, \mathfrak{H} is Laplace operator; if $\eta - \rho_0 c_0 \varepsilon < 0$, \mathfrak{H} is modified Helmholtz operator.

Next the collocation Trefftz method (CTM) in conjunction with composite multiple reciprocity method (CMRM) is implemented to solve simplified time-independent non-homogeneous problems (13)–(14) via boundary nodes. The corresponding Laplace-domain solution can be expressed as

$$\tilde{v}(\mathbf{y}, \varepsilon) = \tilde{v}_h(\mathbf{y}, \varepsilon) + \tilde{v}_p(\mathbf{y}, \varepsilon) \tag{15}$$

where $\tilde{v}_h(\mathbf{y}, \varepsilon)$ and $\tilde{v}_p(\mathbf{y}, \varepsilon)$ represent the homogeneous and the particular solution, respectively. If the particular solution $\tilde{v}_p(\mathbf{y}, \varepsilon)$ satisfies

$$\mathfrak{H}\tilde{v}_p(\mathbf{y}, \varepsilon) = \tilde{W}(\mathbf{y}, \varepsilon) \tag{16}$$

then the homogeneous solution can be solved by the corresponding homogeneous equation

$$\mathfrak{H}\tilde{v}_h(\mathbf{y}, \varepsilon) = 0 \tag{17}$$

with the updated boundary conditions

$$\tilde{v}_h(\mathbf{y}, \varepsilon) = D(\mathbf{y}, \varepsilon) - \tilde{v}_p(\mathbf{y}, \varepsilon) \tag{18a}$$

$$\begin{aligned} -\mathbf{k}\left[\sqrt{f\left((\mathbf{k}^-)^{-1}\mathbf{y}\right)}\nabla\tilde{v}_h(\mathbf{y}, \varepsilon) - \tilde{v}_h(\mathbf{y}, \varepsilon)\nabla\left(\sqrt{f\left((\mathbf{k}^-)^{-1}\mathbf{y}\right)}\right)\right] \cdot \mathbf{n} \\ = E(\mathbf{y}, \varepsilon) + \mathbf{k}\left[\sqrt{f\left((\mathbf{k}^-)^{-1}\mathbf{y}\right)}\nabla\tilde{v}_p(\mathbf{y}, \varepsilon) - \tilde{v}_p(\mathbf{y}, \varepsilon)\nabla\left(\sqrt{f\left((\mathbf{k}^-)^{-1}\mathbf{y}\right)}\right)\right] \cdot \mathbf{n} \end{aligned} \tag{18b}$$

Let us get back to Eq. (16) for evaluating the particular solution $\tilde{v}_p(\mathbf{y}, \varepsilon)$. In the CMRM, it applies the composite differential operators to both sides of Eq. (16) under the assumption of the smooth-enough functions $\tilde{v}_p(\mathbf{y}, \varepsilon)$ and $\tilde{W}(\mathbf{y}, \varepsilon)$, and then vanishes nonhomogeneous term $\tilde{W}(\mathbf{y}, \varepsilon)$ by iterative differentiations

$$\lim_{m \rightarrow \infty} L_m \dots L_2 L_1 \left\{ \tilde{W}(\mathbf{y}, \varepsilon) \right\} \rightarrow 0, \tag{19}$$

where L_1, L_2, \dots, L_m are differential operators of the same or different kinds. Under the assumption that the annihilation (19) is finite order or is truncated at certain order M , the representation can be modified as the following higher order homogeneous equation

$$L_M \dots L_2 L_1 \mathfrak{H}\tilde{v}_p(\mathbf{y}, \varepsilon) \cong 0, \quad \mathbf{y} \in \Omega. \tag{20}$$

To guarantee the uniqueness of the solution, the following constraint conditions are imposed

$$\begin{cases} \mathfrak{H}\tilde{v}_p(\mathbf{y}, \varepsilon) = \tilde{W}(\mathbf{y}, \varepsilon) \\ L_1 \mathfrak{H}\tilde{v}_p(\mathbf{y}, \varepsilon) = L_1 \tilde{W}(\mathbf{y}, \varepsilon) \\ \vdots \\ L_{M-1} \dots L_2 L_1 \mathfrak{H}\tilde{v}_p(\mathbf{y}, \varepsilon) = L_{M-1} \dots L_2 L_1 \tilde{W}(\mathbf{y}, \varepsilon) \end{cases}, \quad \mathbf{y} \in \partial\Omega \tag{21}$$

To solve Eqs. (20)–(21), the particular solution $\tilde{v}_p(\mathbf{y}, \varepsilon)$ can be approximated by a sum of higher order homogeneous solutions,

$$\tilde{v}_p(\mathbf{y}, \varepsilon) = \sum_{i=1}^m \tilde{v}_h^i \tag{22}$$

where \tilde{v}_h^i represents the i th-order composite homogeneous solutions. Then the solution of nonhomogeneous problem (13)–(14) can be represented by $\tilde{v}(\mathbf{y}, \varepsilon) = \sum_{i=0}^M \tilde{v}_h^i$, where $\tilde{v}_h^0 = \tilde{v}_p(\mathbf{y}, \varepsilon)$.

For 2D problems, the i th-order homogeneous solutions \tilde{v}_h^i can be approximated by a linear combination of i th-order Trefftz functions with unknown coefficients $\{a_j^i\}$

$$\tilde{v}_h^i = \sum_{j=1}^N a_j^i u_j^{Ti}(r_y, \theta_y), \quad \mathbf{y} = (r_y \cos \theta_y, r_y \sin \theta_y) \tag{23}$$

where N represents the number of boundary collocation nodes, u_j^{Ti} denotes j th term of Trefftz function satisfying the i th-order homogeneous Eq. (20), one may find the different types of high-order Trefftz functions in ‘‘Appendix’’. And the unknown coefficients $\{a_j^i\}$ can be determined by imposing the boundary conditions (18) and constraint conditions (21).

For 3D problems, the directional Trefftz functions are constructed by using the following variable transformation $\vartheta := q_2 y_2 + q_3 y_3$, where $q_2^2 + q_3^2 = 1$. And then 3D Cartesian coordinates (y_1, y_2, y_3) can be projected into two-dimensional polar coordinates $(r^*, \theta^*) := \left(\sqrt{y_1^2 + (q_2^2 y_2 + q_3^2 y_3)^2}, \arctan\left(\frac{q_2^2 y_2 + q_3^2 y_3}{y_1}\right)\right)$, $i = 1, 2, \dots, M_1$, where $q_2^i = \cos(2i\pi / M_1)$, $q_3^i = \sin(2i\pi / M_1)$ is a direction in the plane (y_2, y_3) , and M_1 denotes the number of

directions. Based on this variable transformation, the aforementioned 2D high-order Trefftz functions can be introduced to solve 3D problems.

Therefore, the i th-order homogeneous solutions \tilde{v}_h^i can be approximated by a linear combination of i th-order directional Trefftz functions with unknown coefficients $\{a_j^i\}$

$$\tilde{v}_h^i = \sum_{j=1}^N a_j^i u_j^{Ti}(r^*, \theta^*), \tag{24}$$

Similar to 2D problem, the unknown coefficients $\{a_j^i\}$ can also be determined by imposing the boundary conditions (18) and constraint conditions (21). After the determination of the coefficients $\{a_j^i\}$, Laplace-domain solution $\tilde{v}(\mathbf{y}, \varepsilon)$ at any point can be evaluated by using Eqs. (23) or (24).

(c) Numerical inverse Laplace transformation

Numerical inverse Laplace transformation (NILT) is implemented to convert the numerical solutions $\tilde{v}(\mathbf{y}, \varepsilon)$ in Laplace space domain to the time-dependent solutions $v_s(\mathbf{y}, t)$ in time domain. Here the well-established Fixed Talbot algorithm [51] is implemented, and the approximate value $v(\mathbf{y}, t)$ for time $t = T$ is given by

$$v_s(\mathbf{y}, T) = \frac{p}{N_{FT}} \left\{ \frac{1}{2} \tilde{v}(\mathbf{y}, p) e^{pT} + \sum_{\mu=1}^{N_{FT}-1} \text{Re} \left[e^{T\omega(\eta_\mu)} \tilde{v}(\mathbf{y}, \omega(\eta_\mu)) (1 + I(\gamma(\eta_\mu))) \right] \right\} \tag{25}$$

where $\omega(\eta_\mu) = p\eta_\mu(\cot \eta_\mu + I)$, $\gamma(\eta_\mu) = \eta_\mu + (\eta_\mu \cot \eta_\mu - 1) \cot \eta_\mu$, $p = \frac{2N_{FT}}{5T}$, $I = \sqrt{-1}$, and $\eta_\mu = \frac{\mu\pi}{N_{FT}}$, $\mu = 1, 2, \dots, N_{FT} - 1$. For a specific time instant T , one may require to solve N_{FT} boundary value problems with the corresponding Laplace transformation parameters $\varepsilon = p$ and $\omega(\eta_\mu)$.

Finally the inverse variable transformation of Eq. (5) is employed to obtain the final time-dependent solution $u(\mathbf{x}, T)$.

2.3 Error analysis

This section presents error analysis of the proposed collocation scheme. In the present implementation procedure, all of Laplace transformation and variable transformation are analytical, and the numerical error appears mainly in the CTM + CMRM implementation of Step (b) and the NILT process of Step (c).

First, we discuss the numerical error generated in Step (c), i.e., Fixed Talbot numerical inverse Laplace transform (NILT). Abate et al. [52, 53] did extensive numerical experiments to investigate the parameter effect on numerical

accuracy. According to his conclusion [53], the following heuristic error estimation of Fixed Talbot algorithm is obtained,

Remark 1 If the error of input data is $\frac{\|\tilde{v}_N - \tilde{v}\|}{\|\tilde{v}\|} \approx 10^{-M_p}$ with positive integer $N_{FT} = M_p$, then the final error is $\left| \frac{v_s - v}{v} \right| \approx 10^{-0.6M_p}$. Therefore the efficiency of the Fixed Talbot algorithm is

$$Eff(FT) = \frac{\text{significant digits obtained}}{\text{precision required}} \approx \frac{0.6M_p}{M_p} \approx 0.6. \tag{26}$$

It can be found from Remark 1 that the Fixed Talbot algorithm tends to demand highly precise input data \tilde{v}_N in order to yield satisfactory accuracy in the following NILT calculations. For this requirement, we implement the collocation Trefftz scheme (CTM) in conjunction with composite multiple reciprocity method (CMRM) in Step (b) to obtain highly accurate solution in Laplace-space domain.

As we can see, the computational error in Step (b) is mainly generated from the CTM + CMRM solution of Laplace-transformed nonhomogeneous problems (13)–(14). Since 3D problems are transformed into 2D problems in the present numerical implementation, the error analysis of the CTM + CMRM in 2D problems is only considered. In the error analysis of the CTM + CMRM, we assume that the solution $\tilde{v} \in H^1(\Omega)$, the source term function \tilde{W} , and the boundary condition function \tilde{g}_1 are smooth enough on Ω . At first, the following homogeneous equation with Dirichlet boundary condition under a polygonal domain is considered

$$\Re \tilde{v} = 0, \tag{27}$$

$$\tilde{v}|_{\partial\Omega} = \tilde{g}_1. \tag{28}$$

When $\Re = \Delta$, we obtain a simplified error estimation from Theorem 3.2 in [54] and maximum principle of Laplace equation [55],

$$\|\tilde{v} - \tilde{v}_N\|_H \leq C_1 \|\tilde{v} - \tilde{v}_N\|_B \leq \frac{C_1 C_2}{N_h^{1/2}}, \tag{29}$$

where $\|\bullet\|$ is the Sobolev norm and H, B denotes the computational domain Ω and its boundary $\partial\Omega$, respectively. And \tilde{v}_N is the corresponding approximation solution, N_h denotes the boundary collocation number on $\partial\Omega$ for obtaining the homogeneous solution, C_1, C_2 are constants independent of N_h .

When $\Re = \Delta + k^2$ and k is not exactly equal (but may be very close) to an eigenvalue $\{\lambda_i\}$ of Laplace operator, we

obtain a simplified error estimation from Corollary 3.1 in [56].

$$\|\tilde{v} - \tilde{v}_{n_1, n_2}\|_H \leq \frac{C_3 N_{h\max}^2}{\delta} \left[\frac{\alpha_+^{n_1+1}}{(n_1 + 1)^{1/2}} + \frac{\alpha_-^{n_2+1}}{(n_2 + 1)^{1/2}} \right], \tag{30}$$

where $\delta = \min_i \left| \frac{k^2 - \lambda_i}{k^2} \right| > 0$ represents the smallest relative distance between k^2 and the eigenvalues λ_i , and the solution domain Ω is divided by a piecewise straight line Γ_I into two subdomains Ω^+ and Ω^- , the solution \tilde{v}_{n_1, n_2} can be represented as

$$\tilde{v}_{n_1, n_2} = \begin{cases} \tilde{v}_{n_1}^+ = a_0^{0+} J_0(kr) + \sum_{i=1}^{n_1} J_i(kr) [a_{2i-1}^{0+} \cos i\theta + a_{2i+1}^{0+} \sin i\theta], & \text{in } \Omega^+ \\ \tilde{v}_{n_2}^- = a_0^{0-} J_0(k\rho) + \sum_{i=1}^{n_2} J_i(k\rho) [a_{2i-1}^{0-} \cos i\theta + a_{2i+1}^{0-} \sin i\theta], & \text{in } \Omega^- \end{cases} \tag{31}$$

and $N_{h\max} = \max\{n_1, n_2\}$, C_3 is a bounded constant independent of $n_1, n_2, k, \delta, \frac{ekr_{\max}^+}{2n_1} \leq \alpha_+ < 1, \frac{ek\rho_{\max}^-}{2n_2} \leq \alpha_- < 1$, in which $r_{\max}^+ = \max_{\text{in}\Omega^+} r, \rho_{\max}^- = \max_{\text{in}\Omega^-} \rho$. Set $\alpha_+ \leq \left(\frac{C_4\delta}{2C_3N_{h\max}^2}\right)^{1/(n_1+1)}$ and $\alpha_- \leq \left(\frac{C_4\delta}{2C_3N_{h\max}^2}\right)^{1/(n_2+1)}$, then the error estimation becomes

$$\begin{aligned} \|\tilde{v} - \tilde{v}_{n_1, n_2}\|_H &\leq \frac{C_3 N_{h\max}^2}{\delta} \left[\frac{\alpha_+^{n_1+1}}{(n_1 + 1)^{1/2}} + \frac{\alpha_-^{n_2+1}}{(n_2 + 1)^{1/2}} \right] \\ &\leq \frac{C_4}{2(n_1 + 1)^{1/2}} + \frac{C_4}{2(n_2 + 1)^{1/2}} < \frac{C_4}{N_{h\min}^{1/2}}, \end{aligned} \tag{32}$$

where the boundary node number $N_{h\min} = \min\{n_1, n_2\}$ for obtaining the homogeneous solution, C_4 is a bounded constant.

Next we turn to the following nonhomogeneous problem

$$\mathfrak{R}\tilde{v} = \tilde{W}, \tag{33}$$

$$\tilde{v}|_{\partial\Omega} = \tilde{g}_1. \tag{34}$$

in which the source term \tilde{W} can be eliminated by using differential operator L_1 , namely, $L_1\{\tilde{W}\} = 0$ on Ω .

Theorem 1 *Let $\tilde{v} = \tilde{v}_h + \tilde{v}_p$ and $\tilde{v}_L = \tilde{v}_{Lh} + \tilde{v}_{Lp}$ be the exact and numerical solution of the nonhomogeneous problem (39)–(40), where \tilde{v}_{Lp} is the particular solution of Eq. (38), and $\mathfrak{R}\tilde{v}_{Lp} = \tilde{W}$. Then*

$$\|\tilde{v} - \tilde{v}_L\|_H \leq \frac{C}{N^{1/2}}, \tag{35}$$

where C is a bounded constant and $N = \min\{N_h, N_p\}$, in which the boundary node number N_p for obtaining the particular solution.

Proof Let \hat{v}_h be the exact solution of the following problem

$$\mathfrak{R}\hat{v}_h = 0, \tag{36}$$

$$\hat{v}_h|_{\partial\Omega} = \tilde{g}_1 - \tilde{v}_{Lp}. \tag{37}$$

Let $\hat{v} = \hat{v}_h + \tilde{v}_{Lp}$, then we have

$$\|\tilde{v} - \tilde{v}_L\|_H \leq \|\tilde{v} - \hat{v}\|_H + \|\hat{v} - \tilde{v}_L\|_H. \tag{38}$$

By using Eqs. (35) or (38), we have

$$\|\hat{v} - \tilde{v}_L\|_H = \|\hat{v}_h - \tilde{v}_{Lh}\|_H \leq \frac{C_h}{N_h^{1/2}}, \tag{39}$$

when $\mathfrak{R} = \Delta, \tilde{v}_{Lh} = \tilde{v}_{N_h}, C_h = C_1 C_2$; when $\mathfrak{R} = \Delta + k^2, \tilde{v}_{Lh} = \tilde{v}_{n_{1h}, n_{2h}}, C_h = C_4, N_h = N_{h\min}$. Notice that in Ω

$$\mathfrak{R}(\tilde{v} - \hat{v}) = \tilde{W} - \hat{W}, \tag{40}$$

and on $\partial\Omega$

$$(\tilde{v} - \hat{v})|_{\partial\Omega} = \tilde{g}_1 - (\tilde{g}_1 - \tilde{v}_{Lp} + \tilde{v}_{Lp}) = 0. \tag{41}$$

According to a priori estimate [55], we obtain

$$\|\tilde{v} - \hat{v}\|_H \leq C_5 \|\tilde{W} - \hat{W}\|_H. \tag{42}$$

Consider the following problems

$$L_1 v = 0, \tag{43}$$

$$v|_{\partial\Omega} = \tilde{W}, \tag{44}$$

where \tilde{W} and \hat{W} are its exact and numerical solution, respectively. For $L_1 = \Delta$, Eq. (42) can be rewritten by using Eq. (29)

$$\|\tilde{v} - \hat{v}\|_H \leq C_5 \|\tilde{W} - \hat{W}\|_H \leq \frac{C_5 C_1 C_2}{N_p^{1/2}}. \tag{45}$$

and then according to Eqs. (38), (39), (45), we get

$$\begin{aligned} \|\tilde{v} - \tilde{v}_L\|_H &\leq \|\tilde{v} - \hat{v}\|_H + \|\hat{v} - \tilde{v}_L\|_H \leq \frac{C_h}{N_h^{1/2}} + \frac{C_5 C_1 C_2}{N_p^{1/2}} \\ &\leq \frac{C}{N^{1/2}}. \end{aligned} \tag{46}$$

For $L_1 = \Delta + k_1^2$ and k_1 is not exactly equal (but may be very close) to an eigenvalue $\{\lambda_i\}$ of Laplace operator, Eq. (42) can be rewritten by using Eq. (32)

$$\|\tilde{v} - \hat{v}\|_H \leq C_5 \|\tilde{W} - \hat{W}\|_H \leq \frac{C_4 C_5}{N_p^{1/2}}. \tag{47}$$

and then according to Eqs. (38), (39), (45), we get

$$\begin{aligned} \|\tilde{v} - \tilde{v}_L\|_H &\leq \|\tilde{v} - \hat{v}\|_H + \|\hat{v} - \tilde{v}_L\|_H \\ &\leq \frac{C_h}{N_h^{1/2}} + \frac{C_4 C_5}{N_p^{1/2}} \leq \frac{C}{N^{1/2}}. \end{aligned} \tag{48}$$

Therefore, the conclusion of the theorem is obtained.

It can be observed from Eq. (35) that the CTM + CMRM has polynomial convergence rate for nonhomogeneous problems (33)–(34), and its error decreases but the condition number of its resultant matrix increases as the boundary node number $N \rightarrow \infty$. In the literatures [9, 38, 44], numerical experiments show that the CTM + CMRM error tends to decrease exponentially and then oscillate slightly below a certain error level with an increase of N .

2.4 Extended precision arithmetic

This section introduces the extended precision arithmetic (EPA) to eliminate the ill-posed issues encountered in the implementation procedure and enhance the applicability of the proposed collocation scheme for transient thermal conduction analysis in large-size-ratio FGMs under heat source loading. Nowadays the common-used double-precision floating point arithmetic ($F = 16$) [42] has the machine epsilon $\varepsilon_M = 2.22\text{E} - 16$, which lead to the following error estimation

$$\varepsilon_N = \varepsilon_M \times \kappa, \tag{49}$$

where ε_N denotes the computational error to measure the numerical accuracy, κ represents the ratio between maximum value and minimum value in the present implementation. To guarantee the numerical error $\varepsilon_N \leq 2.00\text{E} - 02$, the value $\kappa \leq 9.00\text{E} + 13$. Unfortunately, with the increasing size ratio, both the CTM resultant matrix with moderate boundary nodes and the Fixed Talbot algorithm with small term N_{FT} bring very large κ . It could be efficient to implement the EPA in the present implementation. So far, several open source libraries (GMP, MPFR and MPC, etc.) are available for serving on the extended precision arithmetic. Recently, Holoborodko [57] developed an easy-to-implement MATLAB toolbox, Advanpix Multi-precision Computing Toolbox (AMCT). In this study, the AMCT (version 3.9.0.9938) is used in the present computation. More details about the AMCT implementation can be found in Ref. [57].

3 Numerical example

In this section, the numerical accuracy and efficiency of the proposed collocation scheme are verified by 2D/3D

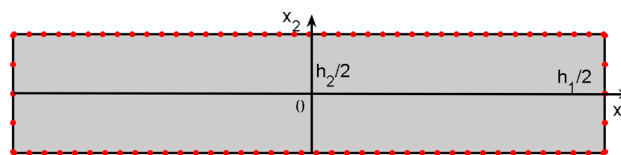


Fig. 3 Schematic configuration of rectangle FGMs with boundary nodes (·) in Example 1

large-size-ratio FGMs with three different types of specific spatial variations (quadratic, exponential and trigonometric functions) under heat source loading. Then the proposed scheme is applied to heat conduction problems under 2D/3D complex-shaped FGMs in comparison to the analytical results and COMSOL results. All the numerical examples are computed on a personal computer with Intel(R) Core(TM) i7-6700 CPU 3.40 GHz and 8 GB RAM. In order to measure the numerical accuracy of the proposed scheme, the relative error $rerr(u)$ and maximum relative error $Mrerr(u)$ is defined as follows,

$$rerr = \left| \frac{u(\mathbf{x}_i, T) - \bar{u}(\mathbf{x}_i, T)}{\bar{u}(\mathbf{x}_i, T)} \right| \tag{50a}$$

$$Mrerr = \text{Max}_{1 \leq i \leq N_T} \left(\left| \frac{u(\mathbf{x}_i, T) - \bar{u}(\mathbf{x}_i, T)}{\bar{u}(\mathbf{x}_i, T)} \right| \right) \tag{50b}$$

where N_T represents the number of test nodes, $u(\mathbf{x}_i)$ and $\bar{u}(\mathbf{x}_i)$ denote the numerical and analytical solutions at test point \mathbf{x}_i with the time instant T , respectively. Unless otherwise specified, the number of boundary nodes $N = N_h = N_p = 91$, the number of directions $M_1 = 13$ in the plane (y_2, y_3), the frequency term in Fixed Talbot algorithm is $N_{FT} = 8$, and the multi-precision floating point arithmetic $F = 30$.

3.1 Numerical verifications

Example 1 Transient thermal conduction with inner heat sources under 2D large-aspect-ratio rectangular FGMs.

Consider transient thermal conduction problems with heat sources in 2D rectangle functionally graded materials $\Omega_1 = \{ (x_1, x_2) | -\frac{h_1}{2} < x_1 < \frac{h_1}{2}, \frac{h_2}{2} < x_2 < \frac{h_2}{2} \}$, which is shown in Fig. 3. The size of FGMs are set as the height $h_2 = 0.1$ and the length $h_1 = h_2 \times SR$, where SR represents the size ratio. Zero initial temperature and full Dirichlet boundary condition are considered in this example. The symbol “ r ” denotes the numerical accuracy less than the engineering accuracy ($Mrerr > 10^{-2}$). The test points are uniformly distributed in the computational domains, and the number of test points $N_T = 121$. Three kinds of FGMs with different types of material variations are investigated.

Case 1.1: 2D FGM with quadratic variations

In this case, the thermal conductivity matrix \mathbf{K} , specific heat $c(\mathbf{x})$ and mass density $\rho(\mathbf{x})$ are quadratic functions, i.e. $f(\mathbf{x}) = (2 + 8x_1 + 2x_2)^2$ in Eqs. (3) and (4), and $\mathbf{k} = \begin{bmatrix} 1 & 1/2 \\ 1/2 & 2 \end{bmatrix}$, $\rho_0 c_0 = 1$. Its analytical temperature distribution can be represented as

$$u(\mathbf{x}, t) = \frac{te^{x_1} \sin x_2}{2 + 8x_1 + 2x_2} \tag{51}$$

and the heat source function $Q(\mathbf{x}, t) = ((t + 1)e^{x_1} \sin x_2 - te^{x_1} \cos x_2)(2 + 8x_1 + 2x_2)$. In the proposed implementation procedure, $\mathbf{k}^- = \begin{pmatrix} 1 & 0 \\ -\sqrt{7}/7 & 2\sqrt{7}/7 \end{pmatrix}$, $\mathfrak{R} = \Delta - \varepsilon$, $\tilde{W} = \frac{e^{y_1}}{\varepsilon^2} \cos\left(\frac{\sqrt{7}y_2 + y_1}{2}\right) - \frac{1+\varepsilon}{\varepsilon^2} e^{y_1} \sin\left(\frac{\sqrt{7}y_2 + y_1}{2}\right)$, and the corresponding annihilating differential operator $L_1 = \Delta$ in Eq. (20).

Case 1.2: 2D FGM with exponential variations

In this case, the thermal conductivity matrix \mathbf{K} , specific heat $c(\mathbf{x})$ and mass density $\rho(\mathbf{x})$ are exponential functions, i.e. $f(\mathbf{x}) = e^{2x_1 + x_2}$ in Eqs. (3) and (4), and $\mathbf{k} = \begin{bmatrix} 1 & 1/2 \\ 1/2 & 2 \end{bmatrix}$, $\rho_0 c_0 = 10^4$. Its analytical temperature distribution can be represented as

$$u(\mathbf{x}, t) = te^{x_1 + 6x_2} \tag{52}$$

and the heat source function $Q(\mathbf{x}, t) = (10^4 - \frac{199t}{2})e^{3x_1 + 7x_2}$. In the proposed implementation procedure, $\mathbf{k}^- = \begin{pmatrix} 1 & 0 \\ -\sqrt{7}/7 & 2\sqrt{7}/7 \end{pmatrix}$, $\mathfrak{R} = \Delta - (10^4\varepsilon + 2)$, $\tilde{W} = \left(\frac{199}{2\varepsilon^2} - \frac{10^4}{\varepsilon}\right)e^{2y_1 + \frac{13(\sqrt{7}y_2 + y_1)}{4}}$, and the corresponding annihilating differential operator $L_1 = \Delta - \frac{185}{4}$ in Eq. (20).

Case 1.3: 2D FGM with trigonometric variations

In this case, the thermal conductivity matrix \mathbf{K} , specific heat $c(\mathbf{x})$ and mass density $\rho(\mathbf{x})$ are trigonometric functions, i.e. $f(\mathbf{x}) = (\sin(x_2 + \pi/4))^2$ in Eqs. (3) and (4), and $\mathbf{k} = \begin{bmatrix} 1 & 0 \\ 0 & 2 \end{bmatrix}$, $\rho_0 c_0 = 10^2$. Its analytical temperature distribution can be represented as

$$u(\mathbf{x}, t) = e^{2x_1} \sqrt{2} \sin\left(x_2 + \frac{3\pi}{4}\right)t \tag{53}$$

and the heat source $Q(\mathbf{x}, t) = (2t + 100)e^{2x_1} \cos 2x_2 \sin(x_2 + \pi/4)$. In the proposed implementation procedure, $\mathbf{k}^- = \begin{pmatrix} 1 & 0 \\ 0 & \sqrt{2}/2 \end{pmatrix}$, $\mathfrak{R} = \Delta - (10^2\varepsilon - 2)$, $\tilde{W} =$

Table 1 Numerical errors obtained by the proposed collocation scheme with/without the EPA in Case 1.1 ($t = 100$ s)

SR	Proposed method ($N = 91$) without EPA ($F = 16$)	Proposed method ($N = 91$) with EPA ($F = 30$)
50	6.85E-7	1.01E-7
100	7.75E-7	1.01E-7
150	1.54E-5	1.01E-7
200	3.26E-6	1.01E-7
250	1.77E-6	1.01E-7
300	2.27E-4	1.01E-7
350	1.67E-3	1.19E-7
400	3.29E-2	5.57E-6
450	/	9.48E-4
500	/	7.87E-2

Table 2 Numerical errors obtained by the proposed collocation scheme with/without the EPA in Case 1.2 ($t = 1000$ s)

SR	Proposed method ($N = 91$) without EPA ($F = 16$)	Proposed method ($N = 91$) with EPA ($F = 30$)
10	7.74E-7	1.01E-7
20	1.03E-7	1.01E-7
30	2.18E-7	1.01E-7
40	2.94E-7	1.01E-7
50	3.71E-5	1.01E-7
60	1.29E-3	1.01E-7
70	1.13E+0	1.01E-7
80	/	1.01E-7
90	/	1.72E-7
100	/	3.09E-5
110	/	6.75E-3
120	/	1.07E+0

$-\frac{(2+10^2\varepsilon)e^{2x_1} \cos 2x_2}{\varepsilon^2}$, and the corresponding annihilating differential operator $L_1 = \Delta$ in Eq. (20).

Tables 1, 2 and 3 list the numerical results obtained by using the proposed collocation scheme with/without the extended precision arithmetic (EPA). It can be found from Tables 1, 2 and 3 that the proposed method with the EPA can enhance the applicability for the large-aspect-ratio FGMs with larger SR, in particular the FGMs with exponential and trigonometric material variations. It indicates that the EPA can alleviate the effect of ill-posed issues generated from the ill-conditioning resultant matrix, the NILT process and the large-size-ratio computational domain.

To investigate the effect of N and N_{FT} on numerical accuracy, the proposed collocation scheme with large EPA ($F = 80$) is implemented in the solution of Cases 1.1–1.3. Figure 4 displays the convergence curves of Cases 1.1–1.3 by using the proposed scheme with two different NILT terms ($N_{FT} = 15$

Table 3 Numerical errors obtained by the proposed collocation scheme with/without the EPA in Case 1.3 ($t = 10$ s)

SR	Proposed method ($N = 91$) without EPA ($F = 16$)	Proposed method ($N = 91$) with EPA ($F = 30$)
20	1.02E-7	1.01E-7
40	1.48E-7	1.01E-7
60	3.26E-6	1.01E-7
80	9.60E-4	1.01E-7
100	1.04E-3	1.01E-7
120	1.80E-2	1.01E-7
140	/	1.01E-7
160	/	1.01E-7
180	/	1.88E-7
200	/	3.46E-4
220	/	3.55E-1

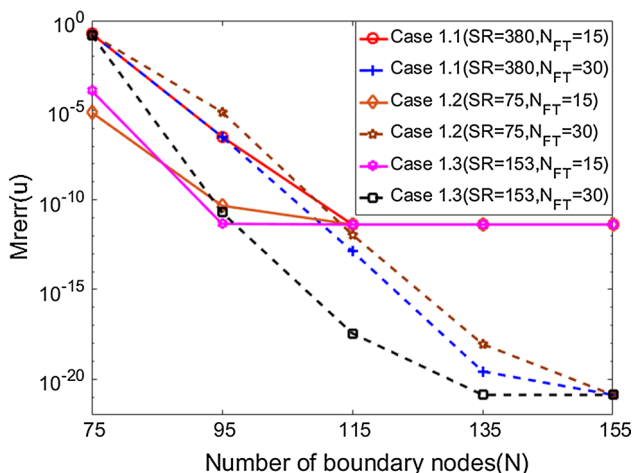


Fig. 4 Convergence curves of Cases 1.1–1.3 by using the proposed scheme with two different NILT terms ($N_{FT}=15$ and 30) under large EPA ($F = 80$)

and 30). It can be observed from Fig. 4 that the proposed method can obtain the satisfactory numerical results with few boundary nodes and converge very fast. Moreover, with small NILT term number $N_{FT}=15$, the numerical accuracy can be improved at the beginning of increasing node number $N(N \leq 115)$, and then it cannot improve any more with the further increasing node number N . This is because the numerical errors are mainly generated from NILT process in the present parameter setting with $N > 115$. At this time, increasing NILT term number becomes the most effective way to improve numerical accuracy.

Example 2 Transient thermal conduction with inner heat sources under 3D large-aspect-ratio cuboid FGMs.

Consider transient thermal conduction problems with heat sources in 3D cuboid FGMs $\Omega_2 = \{(x_1, x_2, x_3) | -\frac{h_1}{2} <$

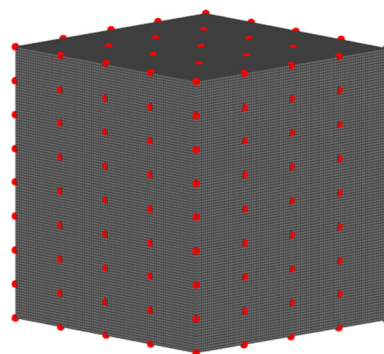


Fig. 5 Schematic configuration of 3D cuboid FGMs with boundary nodes (\cdot) in Example 2

$x_1 < \frac{h_1}{2}, \frac{h_2}{2} < x_2 < \frac{h_2}{2}, \frac{h_3}{2} < x_3 < \frac{h_3}{2}$ }, which is shown in Fig. 5. Set the length and width of 3D FGM $h_1 = h_2 = 0.1$ and the size ratio is defined as $SR = h_3/h_1$, and the number of boundary nodes $N = 162$, the number of test points $N_T = 216$.

Case 2.1: 3D FGM with quadratic variations

In this case, the thermal conductivity matrix \mathbf{K} , specific heat $c(\mathbf{x})$ and mass density $\rho(\mathbf{x})$ are quadratic functions, i.e.

$f(\mathbf{x}) = x_1^2 + 2x_1x_3 + x_3^2$ in Eqs. (3) and (4), and $\mathbf{k} = \begin{bmatrix} 5 & 0 & 0 \\ 0 & 5 & 0 \\ 0 & 0 & 5 \end{bmatrix}$, $\rho_0 c_0 = 10$. Its analytical temperature distribution can be represented as

$u(\mathbf{x}, t) = (x_1 + x_2 - x_3)t$ (54)

and the heat source function $Q(\mathbf{x}, t) = 10(x_1^3 - x_3^3 - x_1x_3^2 + x_2x_3^2 + x_1^2x_2 + x_1^2x_3 + 2x_1x_2x_3)$.

In the proposed implementation procedure, $\mathbf{k}^- = \begin{pmatrix} \sqrt{5}/5 & 0 & 0 \\ 0 & \sqrt{5}/5 & 0 \\ 0 & 0 & \sqrt{5}/5 \end{pmatrix}$, $\mathfrak{R} = \Delta - 10\epsilon$, $\tilde{W} = -\frac{10(x_1^2 - x_3^2 + x_1x_2 + x_3x_2)}{s}$, and the corresponding annihilating differential operator $L_1 = \Delta$ in Eq. (20).

Case 2.2: FGM with exponential variations

In this case, the thermal conductivity matrix \mathbf{K} , specific heat $c(\mathbf{x})$ and mass density $\rho(\mathbf{x})$ are exponential functions, i.e. $f(\mathbf{x}) = e^{0.2x_1 + 0.4x_2 + 0.2x_3}$ in Eqs. (3) and (4), and $\mathbf{k} = \begin{bmatrix} 3 & 0 & 0 \\ 0 & 3 & 0 \\ 0 & 0 & 3 \end{bmatrix}$, $\rho_0 c_0 = 1$. Its analytical temperature distribution

can be represented as

$u(\mathbf{x}, t) = e^{5x_1 + 4x_2 + 0.1x_3 - t}$ (55)

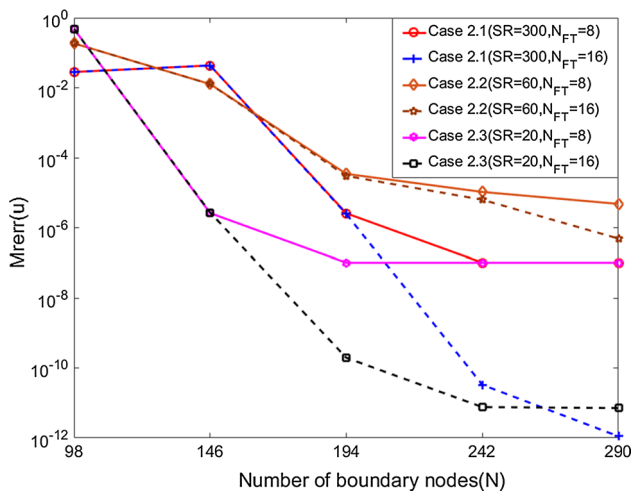


Fig. 6 Convergence curves of Cases 2.1–2.3 by using the proposed scheme with two different NILT terms ($N_{FT}=8$ and 16) under large EPA ($F = 80$)

and the heat source function $Q(\mathbf{x}, t) = -131.89e^{5x_1+4x_2+0.1x_3} e^{-t}$. In the proposed implementation procedure, $\mathbf{k}^- = \begin{pmatrix} \sqrt{3}/3 & 0 & 0 \\ 0 & \sqrt{3}/3 & 0 \\ 0 & 0 & \sqrt{3}/3 \end{pmatrix}$, $\mathfrak{R}=\Delta - (\varepsilon - 0.18)$, $\tilde{W} = -e^{5.1x_1+4.2x_2+0.2x_3} + \frac{131.89e^{5.1x_1+4.2x_2+0.2x_3}}{(\varepsilon+1)}$, and the corresponding annihilating differential operator $L_1 = \Delta - 43.69$ in Eq. (20).

Case 2.3: FGM with trigonometric variations

In this case, the thermal conductivity matrix \mathbf{K} , specific heat $c(\mathbf{x})$ and mass density $\rho(\mathbf{x})$ are trigonometric functions, i.e. $f(\mathbf{x}) = (\cos(x_3) - \sin(x_3))^2$ in Eqs. (3) and (4), and $\mathbf{k} = \begin{bmatrix} 7 & 0 & 0 \\ 0 & 7 & 0 \\ 0 & 0 & 7 \end{bmatrix}$, $\rho_0 c_0=100$, $t = 100$ s. Its analytical temperature distribution can be represented as

$$u(\mathbf{x}, t) = \frac{(x_1x_2 + x_2x_3 + x_1x_3)t}{\sqrt{2} \sin(x_2 + 3\pi/4)} \tag{56}$$

and the heat source function $Q(\mathbf{x}, t) = \sqrt{2}(100 - 7t)(x_1x_2 + x_2x_3 + x_1x_3) \sin(x_2 + 3\pi/4)$. In the proposed implementation procedure, $\mathbf{k}^- = \begin{pmatrix} \sqrt{7}/7 & 0 & 0 \\ 0 & \sqrt{7}/7 & 0 \\ 0 & 0 & \sqrt{7}/7 \end{pmatrix}$, $\mathfrak{R}=\Delta - (10^2\varepsilon - 7)$, $\tilde{W} = \left(\frac{7-100\varepsilon}{\varepsilon^2}\right)(x_1x_2 + x_2x_3 + x_1x_3)$, and the corresponding annihilating differential operator $L_1 = \Delta$ in Eq. (20).

Figure 6 displays the convergence curves of Cases 2.1–2.3 by using the proposed scheme with two different NILT terms ($N_{FT}=8$ and 16). Similar to the conclusion in 2D cases (Example 1), the proposed method can also obtain the sat-

isfactory numerical results with few boundary nodes and converge fast in 3D cases. Numerical errors are mainly generated from NILT process when $N > 194$ in the present parameter setting. At this time, increasing NILT term number becomes the most effective way to improve numerical accuracy. Moreover, Fig. 7 draws temperature distributions and relative errors of 3D cuboid FGMs with different size ratios ($SR = 15, 30, 60$) at time instant ($t = 1$ s) in Case 2.2,

3.2 Application to complex-shaped FGMs

Example 3 Transient thermal conduction analysis in double-head wrench.

Next consider transient thermal conduction in the double-head wrench. Figure 8 shows the real object of the double-head wrench and its simplified computational domain, where h is the opening distance of the wrench. The thermal conductivity matrix \mathbf{K} , specific heat $c(\mathbf{x})$ and mass density $\rho(\mathbf{x})$ of the double-head wrench are quadratic functions, i.e. $f(\mathbf{x}) = (1 + 4x_1 + 2x_2)^2$ in Eqs. (3) and (4), and $\mathbf{k} = \begin{bmatrix} 1 & 1/2 \\ 1/2 & 2 \end{bmatrix}$, $\rho_0 c_0=1$. The initial temperature is assumed to be $u(\mathbf{x}, 0) = 0$, and the full Dirichlet boundary conditions can be obtained by using the following analytical solution

$$u(\mathbf{x}, t) = \frac{\sqrt{2} \sum_{i=1}^{100} e^{\frac{ix_2}{100}} \sin\left(\frac{ix_1}{100} + \frac{\pi}{4}\right) \frac{t}{i}}{1 + 4x_1 + 2x_2} \tag{57}$$

And the source function is

$$Q(\mathbf{x}, t) = -\sqrt{2} \left(\sum_{i=1}^{100} \left(\frac{it}{10^4} - \frac{1}{i} \right) e^{\frac{ix_2}{100}} \sin\left(\frac{ix_1}{100} + \frac{\pi}{4}\right) + \frac{it}{10^4} e^{\frac{ix_2}{100}} \sin\left(\frac{ix_1}{100} + \frac{3\pi}{4}\right) \right) (1 + 4x_1 + 2x_2)$$

In the proposed implementation procedure, $\mathbf{k}^- = \begin{pmatrix} 1 & 0 \\ -\sqrt{7}/7 & 2\sqrt{7}/7 \end{pmatrix}$, $\mathfrak{R}=\Delta - \varepsilon$, $\tilde{W} = \sum_{i=1}^{100} \frac{2i^2 \cos \frac{iy_1}{100} - \varepsilon \left(\cos \frac{iy_1}{100} + \sin \frac{iy_1}{100} \right)}{i\varepsilon^2} e^{\frac{i(\sqrt{7}y_2+y_1)}{200}}$, and the corresponding annihilating differential operator $L_1 = \Delta$ in Eq. (20).

In this example, the accuracy and efficiency of the proposed method are investigated in comparison with the COMSOL simulation. In the COMSOL simulation, two types of the meshes and the adaptive time stepping size are automatically generated by implementing the in-built code, which are shown in Fig. 9. Table 4 lists numerical results obtained by the proposed method and COMSOL software in Example 3 with different h ($h = 1, 1.5, 2$) at $t = 100$ s. Table 5 presents

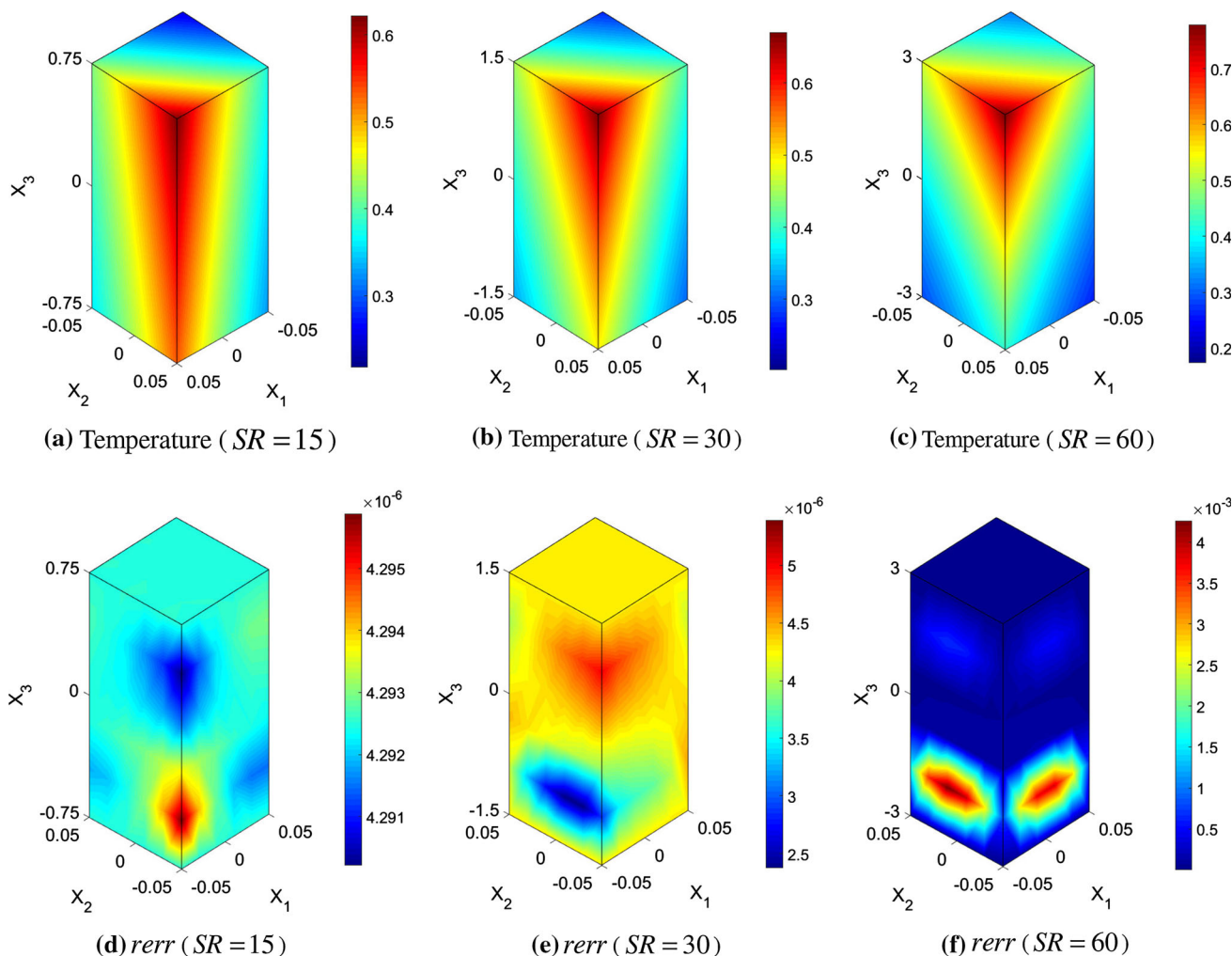


Fig. 7 Temperature distributions and relative errors (rerr) of 3D cuboid FGMs with different size ratios ($SR = 15, 30, 60$) at time instant ($t = 1$ s) in Case 2.2, top row: temperature, **a** $SR = 15$, **b** $SR = 30$, **c** $SR = 60$; bottom row: relative error, **d** $SR = 15$, **e** $SR = 30$, **f** $SR = 60$

numerical comparisons on computational costs of the proposed method and the COMSOL simulation in Example 3. It can be observed from Tables 4 and 5 that the proposed scheme provides more accurate solutions with fewer computational resources than the COMSOL software in Example 3.

Example 4 Transient thermal conduction analysis on the airplane.

To further validate the accuracy of the proposed method, we consider transient thermal conduction on the airplane as shown in Fig. 10. The thermal conductivity matrix \mathbf{K} , specific heat $c(\mathbf{x})$ and mass density $\rho(\mathbf{x})$ of the airplane are quadratic functions, i.e. $f(\mathbf{x}) = x_1^2 - 2x_1x_2 + x_2^2$ in Eqs. (3) and (4), and $\mathbf{k} = \begin{bmatrix} 1 & 1/4 & 1/3 \\ 1/4 & 1 & 1/4 \\ 1/3 & 1/4 & 1 \end{bmatrix}$, $\rho_0 c_0 = 0.01$, $t = 1$ s, and the number of test points $N_T = 834$. The initial temperature and the full

Dirichlet boundary conditions can be obtained by using the following analytical solution

$$u(\mathbf{x}, t) = (x_1 + x_2)t \tag{58}$$

And the source function is

$$Q(\mathbf{x}, t) = \frac{x_1^3 + x_2^3 - x_2^2x_1 - x_1^2x_2}{100}$$

In the proposed implementation procedure, $\mathbf{k}^- = \begin{pmatrix} 1 & 0 & 0 \\ \sqrt{15}/15 & 4\sqrt{15}/15 & 0 \\ -4\sqrt{435}/435 & -13\sqrt{435}/870 & 6\sqrt{29}/29 \end{pmatrix}$, $\mathfrak{R} = \Delta - 0.01\epsilon$, $\tilde{W} = -\frac{(x_1^2 - x_2^2)}{100\epsilon}$, and the corresponding annihilating differential operator $L_1 = \Delta$ in Eq. (20). In addition, the number of boundary nodes $N = 841$ is considered in this example. Figure 11 plots the numerical and analytical temperature distributions on the airplane

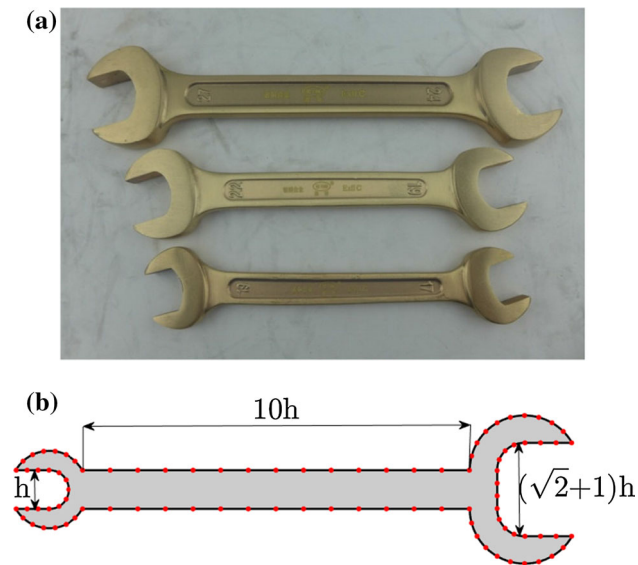


Fig. 8 **a** Real object of the double-head wrench and **b** its simplified computational domain with boundary nodes (·)

surface. Figure 12 displays the relative error of airplane surface, where the maximum relative error appeared in the central region of the wing on both sides is $1.91\text{E}-3$. It reveals that the proposed collocation scheme also works well for transient thermal conduction analysis in 3D FGMs consisting of the size-disparity components.

Finally computation times of the proposed scheme for each example are listed in Table 6. It can be observed from Table 6 that all the present 2D numerical implementations can be done by the proposed collocation scheme in 150 s, and the present 2D numerical implementations can be done by the proposed collocation scheme in 400 s, except for Example 4. This is because the node requirement to well represent the airplane surface is three times more than that of 3D cuboid model.

4 Conclusions

This paper presents a boundary collocation scheme for analyzing transient thermal conduction behavior in large-size-ratio functionally graded materials (FGMs) with heat source load. In the proposed scheme, it employs the Laplace

Table 4 Numerical errors obtained by the proposed method and the COMSOL simulation ($t = 100$ s)

	COMSOL		Proposed method
	Coarse mesh	Refined mesh	
Nodes/elements	388	2337	91
$Mrerr (h = 2)$	$6.78\text{E}-1$	$4.78\text{E}-2$	$2.04\text{E}-5$
$Mrerr (h = 1.5)$	$8.27\text{E}-2$	$2.65\text{E}-3$	$1.01\text{E}-7$
$Mrerr (h = 1)$	$1.25\text{E}-3$	$1.64\text{E}-5$	$1.01\text{E}-7$
CPU time (s)	$7.70\text{E}+1$	$1.25\text{E}+2$	$6.80\text{E}+1$

transformation (LT) and the numerical inverse Laplace transformation (NILT) to convert the problem between time domain and Laplace-space domain to avoid the troublesome time-stepping effect. The boundary-only collocation scheme including the collocation Trefftz method and the composite multiple reciprocity method is implemented in the solution of Laplace-domain nonhomogeneous problems. More importantly, it introduces the extended precision arithmetic to alleviate the effect of ill-posed issues generated from the ill-conditioning resultant matrix, the NILT process and the large-size-ratio computational domain.

Heuristic error analysis and numerical investigation are presented to demonstrate that the proposed method with the EPA can enhance the applicability for the slender FGMs with larger SR, in particular the FGMs with exponential and trigonometric material variations. The proposed method can obtain the satisfactory results with few boundary nodes for complex-shaped FGMs with large size ratio, which requires less computational resource than the method used in the COMSOL simulation. Therefore the proposed collocation scheme can be considered as a competitive alternative for transient thermal conduction analysis in 2D/3D complex-shaped FGMs with large size ratio under heat source loading.

It is worth noting that the rigorous theoretical analysis of the proposed collocation scheme needs to be derived. In addition, this study only considers the thermal conductivity and the product of mass density and specific heat have the same special function variation, namely, the thermal diffusivity is a matrix with constant elements. This assumption allows the development of the proposed boundary collocation scheme without any domain discretization for thermal conduction analysis. Moreover, this method can provide benchmark solu-

Fig. 9 **a** Coarse and **b** refined meshes in the COMSOL simulation

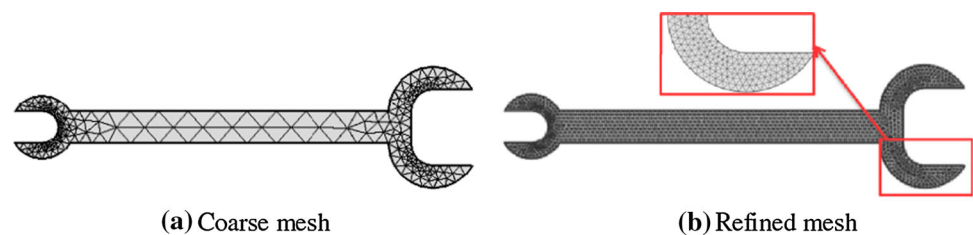


Table 5 Numerical comparisons on computational costs of the proposed method and the COMSOL simulation in Example 3 ($t = 100$ s)

	COMSOL (refined mesh)			Proposed method		
	Elements	$Mrerr$	CPU time (s)	Nodes	$Mrerr$	CPU time (s)
$h = 2$	2337	4.78E-2	1.25E+2	75	8.09E-2	4.90E+1
$h = 1.5$	2337	2.65E-3	1.25E+2	67	2.30E-3	3.80E+1
$h = 1$	2337	1.64E-5	1.25E+2	53	1.58E-5	2.70E+1

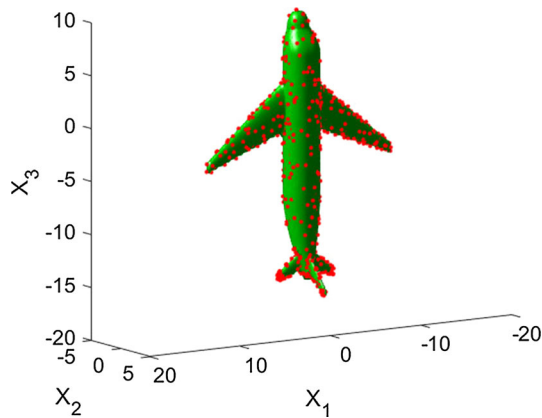


Fig. 10 Schematic configuration of the airplane with boundary nodes (·) in Example 4

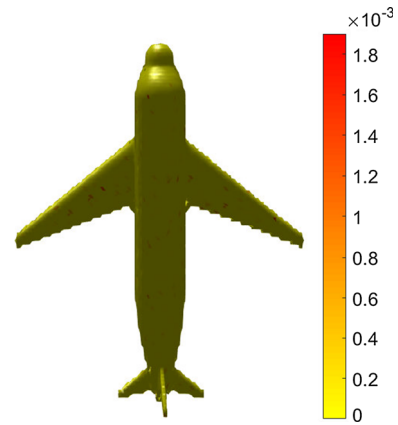
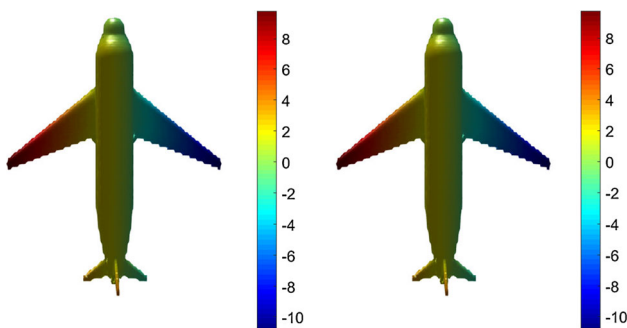


Fig. 12 Relative error distribution on the airplane surface



(a) Numerical solutions **(b)** Analytical solutions

Fig. 11 Temperature distributions on the airplane surface, **a** numerical solutions and **b** analytical solutions

tions to other numerical methods. If thermal diffusivity is not a constant matrix, some additional approaches related to nonlinear problems, such as analog equation method, domain decomposition method, dual reciprocity method and so on, should be introduced. These issues are still under study and will be reported in a subsequent paper.

Acknowledgements The authors thank the anonymous reviewers of this article for their very helpful comments and suggestions to significantly improve the academic quality of this article. The work described in this paper was supported by the National Science Funds of China (Grant No. 11772119), the Fundamental Research Funds for the Central Universities (Grant No. 2016B06214), the Foundation for Open Project of State Key Laboratory of Structural Analysis for Industrial Equipment (Grant No. GZ1707), Qing Lan Project.

Table 6 Computational times of the proposed scheme for each example

Example	Computational time (s)
1.1	29
1.2	142
1.3	34
2.1	304
2.2	356
2.3	313
3	68
4	2733

Appendix

Consider a two-dimensional problem with the domain

$$\Omega = \{(r, \theta) | 0 \leq r < R, 0 \leq \theta \leq 2\pi\} \tag{A1}$$

where r, θ denote the polar coordinates in 2D problems, it can be generated from the Cartesian coordinates (x, y) with the origin at the center of 2D computational domain $\mathbf{x}_c = (x_c, y_c)$, namely, $r = \sqrt{(x - x_c)^2 + (y - y_c)^2}$ and $\theta = \arctan\left(\frac{y - y_c}{x - x_c}\right)$. The high-order Trefftz functions of common-used operators are listed as follows:

- (i) High-order Trefftz functions of Laplacian operator Δ^{n+1}

For Laplace equation $\Delta u = 0$, when $n = 0$, its Trefftz function are given in the literature as

$$1, r^m \cos(m\theta), r^m \sin(m\theta) \quad m = 1, 2, \dots, \quad (r, \theta) \in \Omega \quad (\text{A2})$$

which are known as zero-order Trefftz function u^{T0} . The corresponding n th order Trefftz function u^{Tn} is presented as follows

$$A_n r^{2n}, A_n r^{m+2n} \cos(m\theta), \\ A_n r^{m+2n} \sin(m\theta) \quad m = 1, 2, \dots, \quad (r, \theta) \in \Omega \quad (\text{A3})$$

where $A_n = \frac{A_{n-1}}{4n(m+n)}$, $A_0 = 1$.

(ii) High-order Trefftz functions of Helmholtz operator $(\Delta + \lambda^2)^{n+1}$

In the Helmholtz operator, $\lambda > 0$ is a real number and assume that λ^2 is not an eigenvalue of Laplace operator. Then the zero-order Trefftz function u^{T0} can be written as

$$J_0(\lambda r), J_0(\lambda r) \cos(m\theta), \\ J_0(\lambda r) \sin(m\theta) \quad m = 1, 2, \dots, \quad (r, \theta) \in \Omega \quad (\text{A4})$$

where J_0 is the Bessel function of the first kind. And the following functions are the corresponding n th order Trefftz functions u^{Tn} .

$$A_n (\lambda r)^n J_n(\lambda r), A_n (\lambda r)^n J_{m+n}(\lambda r) \cos(m\theta), \\ A_n (\lambda r)^n J_{m+n}(\lambda r) \sin(m\theta), \quad m = 1, 2, \dots, \quad (r, \theta) \in \Omega \quad (\text{A5})$$

where $A_n = \frac{A_{n-1}}{2n\lambda^2}$, $A_0 = 1$.

(iii) High-order Trefftz functions of modified Helmholtz operator $(\Delta - \lambda^2)^{n+1}$

In the modified Helmholtz operator, λ is again a real number and $\lambda > 0$. Then the zero-order Trefftz function u^{T0} can be given in the form

$$I_0(\lambda r), I_0(\lambda r) \cos(m\theta), \\ I_0(\lambda r) \sin(m\theta) \quad m = 1, 2, \dots, \quad (r, \theta) \in \Omega \quad (\text{A6})$$

where I_0 is the Bessel and Hankel functions with a purely imaginary argument. The corresponding n th order Trefftz function u^{Tn} is presented as follows

$$A_n (\lambda r)^n I_n(\lambda r), A_n (\lambda r)^n I_{m+n}(\lambda r) \cos(m\theta), \\ A_n (\lambda r)^n I_{m+n}(\lambda r) \sin(m\theta), \quad m = 1, 2, \dots, \quad (r, \theta) \in \Omega \quad (\text{A7})$$

where $A_n = \frac{A_{n-1}}{2n\lambda^2}$, $A_0 = 1$.

References

- Zhao X, Liew KM (2010) A mesh-free method for analysis of the thermal and mechanical buckling of functionally graded cylindrical shell panels. *Comput Mech* 45:297–310
- Tian JH, Jiang K (2018) Heat conduction investigation of the functionally graded materials plates with variable gradient parameters under exponential heat source load. *Int J Heat Mass Transf* 122:22–30
- Thai CH, Tran DT, Nguyen-Xuan H (2017) A naturally stabilized nodal integration meshfree formulation for thermo-mechanical analysis of functionally graded material plates. In: *International conference on advances in computational mechanics*, pp 615–629
- Miao Y, Wang Q, Zhu H, Li Y (2014) Thermal analysis of 3D composites by a new fast multipole hybrid boundary node method. *Comput Mech* 53:77–90
- Qian LF, Batra RC (2005) Three-Dimensional transient heat conduction in a functionally graded thick plate with a higher-order plate theory and a meshless local Petrov–Galerkin method. *Comput Mech* 35:214–226
- Zhang HH, Han SY, Fan LF, Huang D (2018) The numerical manifold method for 2D transient heat conduction problems in functionally graded materials. *Eng Anal Bound Elem* 88:145–155
- Wang H, Qin QH, Kang YL (2006) A meshless model for transient heat conduction in functionally graded materials. *Comput Mech* 38:51–60
- Krahulec S, Sladek J, Sladek V, Hon YC (2016) Meshless analyses for time-fractional heat diffusion in functionally graded materials. *Eng Anal Bound Elem* 62:57–64
- Zhou SW, Zhuang XY, Zhu HH, Rabczuk T (2018) Phase field modelling of crack propagation, branching and coalescence in rocks. *Theor Appl Fract Mec* 96:174–192
- Fu ZJ, Chen W, Yang HT (2013) Boundary particle method for Laplace transformed time fractional diffusion equations. *J Comput Phys* 235:52–66
- Sutradhar A, Paulino GH, Gray LJ (2002) Transient heat conduction in homogeneous and non-homogeneous materials by the Laplace transform Galerkin boundary element method. *Eng Anal Bound Elem* 26:119–132
- Fu ZJ, Reutskiy S, Sun HG, Ma J, Khan MA (2019) A robust kernel-based solver for variable-order time fractional PDEs under 2D/3D irregular domains. *Appl Math Lett* 94:105–111
- Abreu AI, Canelas A, Mansur WJ (2013) A CQM-based BEM for transient heat conduction problems in homogeneous materials and FGMs. *Appl Math Model* 37:776–792
- Kielhorn L, Schanz M (2010) Convolution quadrature method-based symmetric Galerkin boundary element method for 3-d elastodynamics. *Int J Numer Methods Eng* 76:1724–1746
- Li Y, Zhang JM, Xie GZ, Zheng XS, Guo SP (2014) Time-domain BEM analysis for three-dimensional elastodynamic problems with initial conditions. *Comput Model Eng Sci* 101:187–206
- Cho JR, Ha DY (2002) Optimal tailoring of 2D volume-fraction distributions for heat-resisting functionally graded materials using FDM. *Comput Methods Appl Mech Eng* 191:3195–3211
- Brian PLT (2010) A finite-difference method of high-order accuracy for the solution of three-dimensional transient heat conduction problems. *AIChE J* 7:367–370
- Wang H, Lei YP, Wang JS, Qin QH, Xiao Y (2015) Theoretical and computational modeling of clustering effect on effective thermal conductivity of cement composites filled with natural hemp fibers. *J Compos Mater* 50:1509–1521
- Mijuca D, Žibera A, Medjo B (2007) A novel primal-mixed finite element approach for heat transfer in solids. *Comput Mech* 39:367–379

20. Olatunji-Ojo AO, Boetcher SKS, Cundari TR (2012) Thermal conduction analysis of layered functionally graded materials. *Comput Mater Sci* 54:329–335
21. Sarler B, Mencinger J (1999) Solution of temperature field in DC cast aluminium alloy billet by the dual reciprocity boundary element method. *Int J Numer Methods Heat Fluid Flow* 9:269–297
22. Feng WZ, Yang K, Cui M, Gao XW (2016) Analytically-integrated radial integration BEM for solving three-dimensional transient heat conduction problems. *Int Commun Heat Mass Transf* 79:21–30
23. Yang K, Peng HF, Wang J, Xing CH, Gao XW (2017) Radial integration BEM for solving transient nonlinear heat conduction with temperature-dependent conductivity. *Int J Heat Mass Transf* 108:1551–1559
24. Qu WZ, Chen W (2015) Solution of two-dimensional stokes flow problems using improved singular boundary method. *Adv Appl Math Mech* 7:13–30
25. Li JP, Fu ZJ, Chen W (2016) Numerical investigation on the obliquely incident water wave passing through the submerged breakwater by singular boundary method. *Comput Math Appl* 71:381–390
26. Fu ZJ, Chen W, Wen PH, Zhang CZ (2018) Singular boundary method for wave propagation analysis in periodic structures. *J Sound Vib* 425:170–188
27. Sarler B (1996) Boundary integral formulation of general source-based method for convective-diffusive solid-liquid phase change problems. *Bound Elem* 18:551–560
28. Sun Y (2017) Indirect boundary integral equation method for the Cauchy problem of the Laplace equation. *J Sci Comput* 71:469–498
29. Chen LC, Li XL (2019) Boundary element-free methods for exterior acoustic problems with arbitrary and high wavenumbers. *Appl Math Model* 72:85–103
30. Chen LC, Liu X, Li XL (2019) The boundary element-free method for 2D interior and exterior Helmholtz problems. *Comput Math Appl* 77:846–864
31. Zhou FL, Yuan L, Zhang JM, Cheng H, Lu CJ (2015) A time step amplification method in boundary face method for transient heat conduction. *Int J Heat Mass Transf* 84:671–679
32. Li M, Chen CS, Chu CC, Young DL (2014) Transient 3D heat conduction in functionally graded materials by the method of fundamental solutions. *Eng Anal Bound Elem* 45:62–67
33. Lin J, Zhang CZ, Sun LL, Lu J (2018) Simulation of seismic wave scattering by embedded cavities in an elastic half-plane using the novel singular boundary method. *Adv Appl Math Mech* 10:322–342
34. Tang ZC, Fu ZJ, Zheng DJ, Huang JD (2018) Singular boundary method to simulate scattering of SH wave by the canyon topography. *Adv Appl Math Mech* 10:912–924
35. Wang FJ, Hua QS, Liu CS (2018) Boundary function method for inverse geometry problem in two-dimensional anisotropic heat conduction equation. *Appl Math Lett* 84:130–136
36. Li JP, Fu ZJ, Chen W, Liu XT (2019) A dual-level method of fundamental solutions in conjunction with kernel-independent fast multipole method for large-scale isotropic heat conduction problems. *Adv Appl Math Mech* 11:501–517
37. O'Hara P, Duarte CA, Eason T, Garzon J (2013) Efficient analysis of transient heat transfer problems exhibiting sharp thermal gradients. *Comput Mech* 51:743–764
38. Gu Y, He XQ, Chen W, Zhang CZ (2017) Analysis of three-dimensional anisotropic heat conduction problems on thin domains using an advanced boundary element method. *Comput Math Appl* 75:33–44
39. Gao XW, Zhang JB, Zheng BJ, Zhang C (2016) Element-subdivision method for evaluation of singular integrals over narrow strip boundary elements of super thin and slender structures. *Eng Anal Bound Elem* 66:145–154
40. Zhou H, Niu Z, Cheng C, Guan Z (2008) Analytical integral algorithm applied to boundary layer effect and thin body effect in BEM for anisotropic potential problems. *Comput Struct* 86:1656–1671
41. Sarra SA, Cogar S (2017) An examination of evaluation algorithms for the RBF method. *Eng Anal Bound Elem* 75:36–45
42. Kansa EJ, Holoborodko P (2017) On the ill-conditioned nature of $C \infty$ RBF strong collocation. *Eng Anal Bound Elem* 78:26–30
43. Fu ZJ, Xi Q, Chen W, Cheng AH-D (2018) A boundary-type meshless solver for transient heat conduction analysis of slender functionally graded materials with exponential variations. *Comput Math Appl* 76:760–773
44. Fu ZJ, Chen W, Qin QH (2012) Three boundary meshless methods for heat conduction analysis in nonlinear FGMs with Kirchhoff and Laplace transformation. *Adv Appl Math Mech* 4:519–542
45. Movahedian B, Boroomand B, Soghrafi S (2013) A Trefftz method in space and time using exponential basis functions: application to direct and inverse heat conduction problems. *Eng Anal Bound Elem* 37:868–883
46. Wei X, Chen W, Chen B, Sun LL (2015) Singular boundary method for heat conduction problems with certain spatially varying conductivity. *Comput Math Appl* 69:206–222
47. Sutradhar A, Paulino GH (2004) The simple boundary element method for transient heat conduction in functionally graded materials. *Comput Methods Appl Mech Eng* 193:4511–4539
48. Sladek J, Sladek V, Zhang C (2004) A local BIEM for analysis of transient heat conduction with nonlinear source terms in FGMs. *Eng Anal Bound Elem* 28:1–11
49. Chen W, Fu ZJ, Qin QH (2009) Boundary particle method with high-order Trefftz functions. *Comput Mater Contin* 13:201–217
50. Li GY, Guo SP, Zhang JM, Li Y, Han L (2015) Transient heat conduction analysis of functionally graded materials by a multiple reciprocity boundary face method. *Eng Anal Bound Elem* 60:81–88
51. Valkó PP, Abate J (2005) Numerical inversion of 2-D Laplace transforms applied to fractional diffusion equations. *Appl Numer Math* 53:73–88
52. Abate J, Valkó PP (2004) Multi-precision Laplace transform inversion. *Int J Numer Meth Eng* 60:979–993
53. Abate J, Whitt W (2006) A unified framework for numerically inverting Laplace transforms. *INFORMS J Comput* 18:408–421
54. Li ZC, Lu TT, Huang HT, Cheng HD (2009) Error analysis of Trefftz methods for Laplace's equations and its applications. *Comput Model Eng Sci* 5252:39–8139
55. Gilbarg D, Trudinger NS (1977) Elliptic partial differential equations of second order. Springer, New York
56. Li ZC (2008) The Trefftz method for the Helmholtz equation with degeneracy. *Appl Numer Math* 58:131–159
57. <http://www.advanpix.com>. Multi-precision computing toolbox for MATLAB. In: Advanpix LLC, Yokohama, 2008–2018

Publisher's Note Springer Nature remains neutral with regard to jurisdictional claims in published maps and institutional affiliations.